

This is an Open Access document downloaded from ORCA, Cardiff University's institutional repository:<https://orca.cardiff.ac.uk/id/eprint/97000/>

This is the author's version of a work that was submitted to / accepted for publication.

Citation for final published version:

Fagereng, Ake and den Hartog, Sabine A. M. 2017. Subduction megathrust creep governed by pressure solution and frictional-viscous flow. *Nature Geoscience* 10 (1) , pp. 51-57. 10.1038/ngeo2857

Publishers page: <http://dx.doi.org/10.1038/ngeo2857>

Please note:

Changes made as a result of publishing processes such as copy-editing, formatting and page numbers may not be reflected in this version. For the definitive version of this publication, please refer to the published source. You are advised to consult the publisher's version if you wish to cite this paper.

This version is being made available in accordance with publisher policies. See <http://orca.cf.ac.uk/policies.html> for usage policies. Copyright and moral rights for publications made available in ORCA are retained by the copyright holders.



1   **Subduction megathrust creep governed by pressure solution and**  
2   **frictional-viscous flow**

3   Åke Fagereng<sup>1,2,\*</sup> & Sabine A. M. den Hartog<sup>3,4</sup>

4   <sup>1</sup>*School of Earth & Ocean Sciences, Cardiff University, Cardiff, CF10 3AT, United*  
5   *Kingdom.*

6   <sup>2</sup>*Department of Geological Sciences, University of Cape Town, Private Bag X3,*  
7   *Rondebosch 7701, South Africa.*

8   <sup>3</sup>*HPT Laboratory, Department of Earth Sciences, Utrecht University, Utrecht, The*  
9   *Netherlands.*

10   <sup>4</sup>*Now at: Rock Deformation Laboratory, School of Environmental Sciences, University*  
11   *of Liverpool, Liverpool, United Kingdom*

12   \*Corresponding author: FagerengA@cardiff.ac.uk

13   **Subduction megathrust slip speeds range from slow creep at plate convergence**  
14   **rates (centimetres per year) to seismic slip rates (metres per second) in the largest**  
15   **earthquakes on Earth. The deformation mechanisms controlling whether fast slip**  
16   **or slow creep occurs, however, remain unclear. Here, we present evidence that**  
17   **pressure solution creep - fluid-assisted, stress-driven mass transfer - is an**  
18   **important deformation mechanism in megathrust faults. We quantify megathrust**  
19   **strength using a laboratory-constrained microphysical model for fault friction,**  
20   **involving viscous pressure solution and frictional sliding. We find that at plate-**  
21   **boundary deformation rates, aseismic, frictional-viscous flow is the preferred**

22 **deformation mechanism at temperatures above 100 °C. The model thus predicts**  
23 **aseismic creep at temperatures much cooler than the onset of crystal plasticity,**  
24 **unless a boundary condition changes. Within this model framework, earthquakes**  
25 **may nucleate when a local increase in strain rate triggers velocity-weakening slip,**  
26 **and we speculate that slip area and event magnitude increase with increasing**  
27 **spacing of strong, topographically derived irregularities in the subduction**  
28 **interface.**

29       Understanding why some megathrust segments accommodate displacement by  
30    earthquake slip versus aseismic creep is a major challenge. Geophysically observed  
31    variation in seismic style along active subduction megathrusts, involving a continuum  
32    of slip speeds from plate boundary creep rates to earthquake slip<sup>1</sup>, arises from processes  
33    within a fault zone in subducting sediments on top of potentially rugged ocean floor<sup>2-6</sup>.  
34    Dominantly creeping margins are characterised by low seismic coupling coefficients -  
35    the observed seismic moment release rate over that required by plate motion vectors -  
36    and lack of earthquake moment magnitudes  $\geq 8.0$  (Supplementary Figure S1)<sup>7,8</sup>. Thus,  
37    some margins produce small to medium magnitude earthquakes, but the total moment of  
38    these earthquakes is insufficient to explain total geodetically observed displacement,  
39    and they must therefore be accompanied by aseismic creep<sup>9</sup>.

40       The megathrust interface is commonly inferred as seismogenic to a depth where  
41    temperature exceeds the 350°C required for crystal plasticity in quartz, or to the  
42    intersection with the hanging wall Moho, whichever is shallower<sup>10</sup>. However, geodetic  
43    inversions<sup>8,11-14</sup> reveal aseismic creep shallower than both the 350°C isotherm and the  
44    hanging wall Moho. The question thus arises: how do some megathrust segments, such

45 as north Hikurangi<sup>11</sup>, the southern Japan Trench<sup>12</sup>, southern New Hebrides<sup>13</sup>, southern  
46 Kermadec Arc<sup>13</sup>, and the Manila Trench<sup>14</sup> accommodate detectable displacement by  
47 aseismic creep in addition to moderate size earthquakes, both originating at a similar  
48 depth range? This observation requires average creep rates of centimetres per year at  
49 temperatures less than 350°C. Identifying the associated creep mechanism is critical for  
50 recognising where megathrust displacement can occur without great earthquakes, and  
51 by contrast, interpret where great earthquakes may occur.

## 52 **The mechanism of creep at seismogenic zone conditions**

53 Tectonic mélanges comprising sheared trench-fill and ocean floor sediments have  
54 been interpreted as megathrust fault rocks (Fig. 1a)<sup>3-6,15</sup>. Deformation structures  
55 developed at seismogenic pressure-temperature ( $P - T$ ) conditions include both  
56 discontinuities, such as faults and tensile fractures, and continuous structures such as  
57 folds, boudins and foliations. One possible interpretation is that faults and associated  
58 fractures represent seismic deformation styles, whereas continuous features characterise  
59 slower, distributed, aseismic mechanisms recorded as creep<sup>5,6,15</sup>. In this interpretation,  
60 the mechanism accommodating deformation in continuous structures is responsible for  
61 aseismic creep.

62 In exhumed subduction thrusts, cleavage defined by fine-grained phyllosilicates  
63 wraps around rigid quartz clasts (Fig. 1b). Comparable microstructures are reported in  
64 borehole samples from the creeping segment of the continental San Andreas transform  
65 fault<sup>16,17</sup>. Mass balance calculations on San Andreas samples indicate pressure solution,  
66 involving fluid-assisted, stress-driven mass transfer, as the cleavage-forming process<sup>16</sup>.

67 If empirical rates can be extrapolated, pressure solution is fast enough to account for  
68 aseismic sliding<sup>16,18</sup>.

69 Pressure solution is also widely inferred as the dominant cleavage-forming  
70 process in mudrocks and phyllites sampled from exhumed subduction thrusts<sup>6,19-21</sup>. As  
71 an example, we consider a sample representative of sheared, cleaved mudstone from an  
72 inferred exhumed megathrust in the Chrystals Beach Complex, New Zealand<sup>21</sup> (Fig. 1a-  
73 e), where cleavage defined by illite-muscovite developed at  $T < 300^{\circ}\text{C}$  (ref. 22). In this  
74 sample, cleavage seams are depleted in Si and enriched in Al (Fig. 1c; Supplementary  
75 Figure 2). If cleavage develops by pressure solution, more soluble elements, such as Si,  
76 are dissolved, whereas less soluble elements, such as Al, are retained. Thus, the  
77 observations in the Chrystals Beach sample are consistent with cleavage formation by  
78 pressure solution. Stress shadows around quartz clasts lack evidence for opening of pore  
79 space (Fig. 1d), and are sites of local silica enrichment (Fig. 1e). In addition to  
80 formation of phyllosilicate cleavage, mass-transfer processes are therefore illustrated by  
81 silica enrichment and clast elongation through mineral growth in pressure shadows (Fig.  
82 1d,e).

### 83 **Microphysical model for fault gouge strength**

84 The observations on exhumed megathrust rocks indicate that one of the  
85 microscopic processes that controls macroscopic frictional behaviour is viscous pressure  
86 solution. Indeed, microphysical modelling studies have shown that experimental  
87 observations on shear deformation at low strain rates in rocks comprising rigid clasts in  
88 a phyllosilicate matrix can be explained by *frictional-viscous flow*: frictional sliding

89 along cleavage planes coupled to viscous (time-dependent) pressure solution of  
90 intervening rigid clasts<sup>23,24,25</sup>. The microstructures reported in these experimental studies  
91 are essentially identical to those seen in samples from the exhumed Chrystalls Beach  
92 Complex (Fig. 1b-e). Frictional-viscous flow is restricted to low strain-rates (and/or  
93 high  $T$ ); at higher strain rates (or lower  $T$ ), slip is activated on anastomosing  
94 phyllosilicates, and microphysical models predict an importance of compaction by  
95 pressure solution<sup>24,25</sup>. Here, we use the model by Den Hartog and Spiers<sup>25</sup>, coupled to  
96 analytical thermal gradients<sup>26</sup>(Methods), to predict megathrust shear strength. This  
97 microphysical model is based on friction experiments performed on materials and at  
98 conditions representative for subduction megathrusts. Following this model, we assume  
99 a matrix-supported megathrust shear zone where frictional sliding occurs on aligned  
100 phyllosilicates, accommodated by pressure solution shear of intervening quartz grains or  
101 dilatation (Fig. 1f). In this model, the relation between shear strain rate and shear stress  
102 is derived by considering stress balances at the microscale for a unit cell defined in Fig.  
103 1f. The megathrust shear strain rate ( $\dot{\gamma}$ ) is related to the slip velocity ( $V$ ) assuming strain  
104 is distributed through a shear zone thickness ( $w$ ) and therefore  $\dot{\gamma} = V/w$ .

105 Each unit cell consists of quartz clasts, which are uniformly distributed such that  
106 horizontal rows overlap, and phyllosilicate foliations that are on average parallel to the  
107 shear plane, but locally curve around rigid clasts (ref. 25; Fig. 1f; Supplementary Figure  
108 3), resembling the natural microstructure (Fig. 1b). Slip along foliation is assumed to be  
109 a frictional process governed by the frictional resistance of phyllosilicates, which varies  
110 with temperature and normal stress according to experimental data for illite and  
111 muscovite<sup>27-31</sup>(Methods). Depending on the conditions (e.g. slip velocity, temperature,  
112 normal stress), the frictional resistance predicted by the model either decreases

113 (velocity-weakening) or increases (velocity-strengthening) as slip accelerates. Whereas  
114 velocity-weakening behaviour is potentially unstable, and can promote fast earthquake  
115 slip, velocity-strengthening behaviour is inferred to lead to stable sliding, recorded as  
116 aseismic creep<sup>32-34</sup>. In the microphysical model used here<sup>25</sup>, velocity-strengthening flow  
117 occurs when easy shear of quartz clasts by thermally activated pressure solution, in  
118 series with rate-independent slip on planar phyllosilicates, leads to non-dilatant  
119 deformation (frictional-viscous flow). Velocity-weakening slip occurs when difficult  
120 pressure solution shear of quartz results in increased shear stress and slip is activated on  
121 curved phyllosilicate cleavages. This slip along curved foliation results in dilatation at  
122 the clast-matrix interface under extension (Fig. 1f), which at steady state is balanced by  
123 compaction via pressure solution.

124 **Application of flow law to natural subduction zones**

125 We apply boundary conditions appropriate for the northern Hikurangi margin, a  
126 megathrust shown to deform predominantly by aseismic creep, at least over the last few  
127 decades<sup>11</sup>. Pore fluid factors ( $\lambda = P_f/\sigma_v$ , where  $P_f$  is pore fluid pressure and  $\sigma_v$  is vertical  
128 stress) of 0.8 and 0.95 are imposed to test variations between moderate and high fluid  
129 pressure conditions. We distribute a steady creep rate of 40 mm yr<sup>-1</sup> over a 1 - 100 m  
130 thick subduction thrust shear zone, a range representing strain rates from  $10^{-11}$  to  $10^{-9}$  s<sup>-1</sup>,  
131 and a range in deforming thickness typical of exhumed mélange and drilled  
132 subduction megathrusts<sup>15</sup>. Quartz grain size varies from 10 to 100  $\mu\text{m}$ , based on Fig. 1b-  
133 e. All model parameters are listed in Supplementary Table S1.

134        The frictional-viscous flow strength of quartz-phyllosilicate mixtures as a function  
135        of depth is compared to frictional strengths of mono-mineralic quartz and illite-  
136        muscovite faults (Fig. 2a,b). At all considered conditions, frictional sliding in quartz  
137        requires higher shear stress than any slip mechanism in phyllosilicates or quartz-  
138        phyllosilicate mixtures; we therefore note that frictional sliding in quartz is an unlikely  
139        deformation mechanism in phyllosilicate-rich megathrust shear zones. For both high  
140        and moderate fluid overpressure, there is a depth below which frictional-viscous flow  
141        requires a lower shear stress than that required for frictional sliding in mono-mineralic  
142        phyllosilicate fault gouges (Fig. 2a,b). For deforming zones of 100 m thickness,  
143        frictional viscous flow becomes favourable at 8 – 10 km depth in moderate fluid  
144        pressure conditions (Fig. 2a), and at 12 – 16 km depth under high fluid pressure (Fig.  
145        2b). In both cases, frictional-viscous flow becomes favourable at  $T \geq 100 \pm 20$  °C (Fig.  
146        2c), where the corresponding shear stress,  $\tau$ , is  $\leq 10$  MPa at high fluid pressure, and  $\leq$   
147        20 MPa at moderate fluid pressure (Fig. 2a,b). For a 1 m thick deforming zone, higher  
148        strain rates make frictional-viscous flow less favourable; at high fluid pressure,  
149        frictional sliding of phyllosilicates remains favourable until a depth of  $\sim 26$  km ( $T < 200$   
150        °C,  $\tau < 20$  MPa), whereas at lower fluid pressures, frictional sliding also requires higher  
151        stresses and frictional-viscous flow becomes favourable from 16 km depth ( $T < 150$  °C,  
152         $\tau \sim 40$  MPa).

153        Calculated temperatures define low thermal gradients, partly because very low  
154        stresses reduce temperatures relative to models with Byerlee friction (Fig. 2c). In our  
155        warmest model, where  $\lambda = 0.8$ , shear zone width is 1 m, and quartz grain size 100 µm,  
156        shear heating makes up approximately 30 % of the heat budget; for the coldest model,

157 with  $\lambda = 0.95$ , shear zone width of 100 m, and quartz grain size 10  $\mu\text{m}$ , less than 10 %  
 158 of the heat budget is contributed by shear heating. Hikurangi is also a cool margin in the  
 159 global spectrum of subduction zone thermal models, where model temperatures<sup>35</sup>  
 160 compare to Fig. 2c. Compared to a recent numerical model<sup>36</sup>, calculations here with  $\lambda =$   
 161 0.8 are cooler at depths below  $\sim 10$  km, whereas  $\lambda = 0.95$  gives consistently lower  
 162 temperatures.

163 Aseismic frictional-viscous flow is the predicted deformation style at  $T \geq 100$  °C,  
 164 when average plate boundary shear strain rates are accommodated in a hundreds of  
 165 metres thick shear zone (Fig. 2a,b). Generation of run-away earthquake slip requires a  
 166 change in these boundary conditions. This is because, at low strain rates, pressure  
 167 solution of quartz clasts accommodates local finite strain around the rigid clasts created  
 168 by slip on surrounding, planar phyllosilicate cleavages (Figs. 1d,e, 3a,b)<sup>25</sup>. At higher  
 169 strain rate, pressure solution requires greater driving stress, bulk fault zone strength  
 170 increases, and eventually dilatant, velocity-weakening behaviour occurs, allowing  
 171 potentially unstable slip<sup>25</sup> (Fig. 3a,b). At each depth increment in Fig. 2, we calculate  
 172 the friction coefficient as a function of strain rate, as shown for a depth of 30 km in Fig  
 173 3b. The strain rate required for a change from velocity-strengthening to velocity-  
 174 weakening behaviour increases with depth (Fig. 3c). At depths greater than 15 km,  
 175 where frictional-viscous flow generally becomes favourable (Fig. 2), velocity-  
 176 strengthening behaviour occurs at strain rates slower than  $10^{-12}$  s<sup>-1</sup> and shear zone  
 177 widths greater than tens of metres at 40 mm yr<sup>-1</sup> slip rates (Fig. 3c). At a depth of 30  
 178 km, where frictional-viscous flow is preferred for all our considered conditions with a  
 179 plate boundary slip rate (Fig. 2a,b), the shear strain rates required for velocity-  
 180 weakening behaviour range from  $10^{-9}$  to  $10^{-4}$  s<sup>-1</sup> (Fig. 3b,c).

181 At shallow depths, although commonly interpreted as a velocity-strengthening  
182 region<sup>10,34</sup>, potentially seismic slip is predicted at strain rates as low as  $10^{-12} \text{ s}^{-1}$  at 5 km  
183 depth, and  $10^{-16} \text{ s}^{-1}$  at the surface (Fig. 3c). This is because shear deformation by  
184 pressure solution of quartz is difficult at low temperature, yielding dilatant behaviour.  
185 At greater depths, where  $T \geq 100 \pm 20^\circ\text{C}$ , low strain rate frictional-viscous flow is the  
186 predicted deformation mechanisms (Fig. 2), because a high quartz solubility yields  
187 efficient dissolution and re-precipitation at this temperature (Ref. 37, Supplementary  
188 Figure 4). This potential change in deformation mechanism is reflected in exhumed  
189 accretionary prisms, where mélange deformation at  $T < 100^\circ\text{C}$  is dominated by  
190 distributed cataclasis, whereas a pressure solution cleavage and localised slip surfaces  
191 are prevalent in rocks deformed at  $T > 150^\circ\text{C}$  (Refs. 6,21,38,39). In central and northern  
192 Hikurangi, the margin we used for our thermal calculations, it is uncertain whether a  
193 near-surface velocity-strengthening zone and updip limit of seismicity is present, as  
194 slow slip events may propagate to the trench<sup>40</sup>; the downdip limit of the interseismically  
195 locked zone is here at less than 10 km depth<sup>11</sup>. This downdip limit of the locked zone is  
196 in agreement with the onset of velocity-strengthening frictional-viscous flow at 10 km  
197 depth and  $T \leq 100^\circ\text{C}$ , in a margin of moderate fluid overpressure and distributed shear  
198 (Fig. 2a,c).

199 Following Den Hartog and Spiers<sup>25</sup>, we conclude that frictional-viscous flow  
200 involving pressure solution is a viable mechanism of velocity-strengthening, stable  
201 creep. We consider the recently discovered phenomenon of slow slip along subduction  
202 megathrusts<sup>41,42</sup>, defined as geodetically observed displacement that is faster than plate  
203 convergence rates but too slow to generate seismic waves, as a form of unstable slip<sup>43</sup>.  
204 Shallow slow slip, as observed near the trench in northern Hikurangi<sup>40</sup>, may therefore be

205 a manifestation of unstable, dilatant shear at  $T < 100^\circ\text{C}$  (the ‘potentially seismic slip’ in  
206 Fig. 3c). Deeper slow slip events occurring down-dip of the locked zone and at depths  $\geq$   
207 30 km, such as in Cascadia, are either independent of, or possibly load, the seismogenic  
208 region<sup>44</sup>. The application of the microphysical model predicts velocity-strengthening  
209 behaviour at such depths; thus, as for earthquakes, slow slip faster than steady-state  
210 plate convergence rates requires a local change in conditions, possibilities of which we  
211 discuss in the next section. Under the local triggering conditions, slow slip likely  
212 reflects competition between deformation modes within a heterogeneous fault zone<sup>45</sup>,  
213 but may be an expression of either localised frictional sliding or distributed shearing  
214 flow; differentiating between these basic geometries requires currently missing  
215 knowledge of the deforming thickness during slow slip events.

216 **Relating creep to subduction of rugged vs. smooth slab topography**

217 Large earthquakes ( $M_w \geq 8.0$ ) have been associated with subduction of smooth sea  
218 floor, because a lack of barriers to slip – such as local topography, seamounts, and  
219 horst-and-graben structures – allows for large rupture areas<sup>2,46</sup>. By comparison,  
220 subduction of rugged ocean floor has been suggested to lead to smaller earthquakes  
221 because rupture areas are geometrically constrained<sup>2,12,36</sup>. We therefore consider the  
222 implications of the model results for two end-member subducting plates, with (i)  
223 smooth and (ii) rugged topography<sup>2,36,46</sup>.

224 (i) Smooth subducting slabs lack geometrical barriers to rupture propagation and  
225 the fault zone has similar thickness and strain rate at all depths (Fig. 4a). However,  
226 small-scale heterogeneities may locally elevate strain rates, causing velocity-weakening

behaviour (Fig. 3b,c), and triggering rupture propagation over a large area without hindrance by large-scale barriers<sup>4</sup>. (ii) Rugged subducting ocean floor also deforms predominantly via creep by frictional-viscous flow, and small-scale heterogeneities may again lead to local velocity-weakening behaviour. However, in this case, strong, topographically derived irregularities on the interface create barriers to earthquake propagation, constraining earthquakes to smaller slip areas and therefore moderate magnitudes (Fig. 4b). At and around such barriers, local brittle deformation occurs to accommodate subduction of the topographic feature<sup>2,12</sup>. Extrapolating from continental strike slip faults<sup>47</sup>, we suggest that geometrical barriers - such as deformed, subducting seamounts - that result in a discontinuity of potential slip surfaces by more than ~ 4 km, are likely to arrest rupture propagation. Moreover, because of numerous stress and strain-rate peaks, megathrusts associated with rugged subducting topography may appear strong in stress calculations from heat flow measurements<sup>36</sup> or Coulomb wedge mechanics<sup>48</sup>, relative to fault segments where smooth subducting slabs allow large slip areas on a through-going weak surface or a system of anastomosing slip surfaces. A caveat to this broad, end-member interpretation is that subducting topography and megathrust structure may evolve with depth. For example, subducting seamounts may be progressively destroyed if they are indeed areas of increased brittle deformation<sup>2</sup>, and the microscale geometry within the fault zone can change through development of through-going fault surfaces, mineral precipitation and reactions, and evolving grain shapes and sizes, through progressive deformation, metamorphism and fluid flow<sup>49</sup>. As such, the subduction thrust is a dynamic structure, displacing a footwall with inherently complex geometry, and accurate predictions require high-resolution subsurface data.

250 In summary, our model offers an explanation for why megathrusts creep in some  
251 places, and slip seismically in others. It implies that creep by frictional-viscous flow is  
252 the preferred deformation mechanism of most if not all subduction thrust interfaces,  
253 below some depth determined by thermal structure, strain rate, and fluid pressure (Figs.  
254 2,3; Supplementary Figure 4). However, earthquakes may nucleate at local  
255 heterogeneities where the behaviour is velocity-weakening<sup>50</sup>. Slip area and earthquake  
256 magnitude should then depend on the spacing of strong, topographically derived  
257 irregularities in the subduction interface, with giant earthquakes requiring this spacing  
258 to be large.

259

## 260 **References**

- 261 1. Peng, Z. & Gomberg, J. An integrated perspective of the continuum between  
262 earthquakes and slow slip phenomena. *Nat. Geosci.* **3**, 599-607 (2010).
- 263 2. Wang, K. & Bilek, S.L. Do subducting seamounts generate or stop large earthquakes?  
264 *Geology* **39**, 819-822 (2011).
- 265 3. Shreve, R.L. & Cloos, M. Dynamics of sediment subduction, mélange formation, and  
266 prism accretion. *J. Geophys. Res.* **91**, 10229-10245 (1986).
- 267 4. Bachmann, R. *et al.* Exposed plate interface in the European Alps reveals fabric  
268 styles and gradients related to an ancient seismogenic coupling zone. *J. Geophys. Res.*  
269 **114**, B05402, doi:10.1029/2008JB005927 (2009).
- 270 5. Fagereng, Å. & Sibson, R.H. Mélange rheology and seismic style. *Geology* **38**, 751-  
271 754 (2010).

- 272 6. Rowe, C.D., Meneghini, F. & Moore, J.C. in *Geology of the Earthquake Source: A*  
273 *Volume in Honour of Rick Sibson* (eds. Fagereng, Å., Toy, V.G. & Rowland, J.V.), 77-  
274 95 (Geol. Soc. London, 2011).
- 275 7. Heuret, A., Lallemand, S., Funiciello, F., Pitomallo, C. & Faccenna, C. Physical  
276 characteristics of subduction interface type seismogenic zones revisited. *Geochem.*  
277 *Geophys. Geosyst.* **12**, Q01004, doi: 10.1029/2010GC003230 (2011).
- 278 8. Scholz, C.H. & Campos, J. The seismic coupling of subduction zones revisited. *J.*  
279 *Geophys. Res.* **117**, B05310, doi:10.1029/2011JB009003 (2012).
- 280 9. Rubin, A.M., Gillard, D. & Got, J.-L. Streaks of microearthquakes along creeping  
281 faults. *Nature* **400**, 635-641 (1999).
- 282 10. Hyndman, R.D., Yamano, M. & Oleskevich, D.A. The seismogenic zone of  
283 subduction thrust faults. *Isl. Arc* **6**, 244-260 (1997).
- 284 11. Wallace, L.M. *et al.* Characterizing the seismogenic zone of a major plate boundary  
285 subduction thrust: Hikurangi Margin, New Zealand. *Geochem. Geophys. Geosyst.* **10**,  
286 Q10006, doi: 10.1029/2009GC002610 (2009).
- 287 12. Mochizuki, K., Yamada, T., Shinohara, M., Yamanaka, Y. & Kanazawa, T. Weak  
288 interplate coupling by seamounts and repeating  $M \sim 7$  earthquakes. *Science* **321**, 1194-  
289 1197 (2008).
- 290 13. Power, W., Wallace, L.M., Wang, X. & Reyners, M. Tsunami hazard posed to New  
291 Zealand by the Kermadec and Southern New Hebrides subduction margins: An  
292 assessment based on plate boundary kinematics, interseismic coupling, and historical  
293 seismicity. *Pure Appl. Geophys.* **169**, 1-36 (2012).

- 294 14. Hsu, Y.-J., Yu, S.-B., Song, T.-R. & Bacolcol, T. Plate coupling along the Manila  
295 subduction zone between Taiwan and northern Luzon. *J. Asian Earth Sci.* **51**, 98-108  
296 (2012).
- 297 15. Rowe, C.D., Moore, J.C., Remitti, F. & IODP Exp. 343/343T Scientists. The  
298 thickness of subduction plate boundary faults from the seafloor into the seismogenic  
299 zone. *Geology* **41**, 991-994 (2013).
- 300 16. Gratier, J.-P. *et al.* Aseismic sliding of active faults by pressure solution creep:  
301 Evidence from the San Andreas Fault Observatory at Depth. *Geology* **39**, 1131-1134  
302 (2011).
- 303 17. Richard, J., Gratier, J.P., Doan, M.-L., Boullier, A.-M. & Renard, F. Rock and  
304 mineral transformations in a fault zone leading to permanent creep: Interactions  
305 between brittle and viscous mechanisms in the San Andreas Fault. *J. Geophys. Res.* **119**,  
306 8132-8153 (2014).
- 307 18. Gratier, J.-P., Guiguet, R., Renard, F., Jenatton, L. & Bernard, D. A pressure  
308 solution creep law for quartz from indentation experiments. *J. Geophys. Res.* **114**,  
309 B03403 (2009).
- 310 19. Schwarz, S. & Stöckhert, B. Pressure solution in siliciclastic HP-LT rocks –  
311 constraints on the state of stress in deep levels of accretionary complexes.  
312 *Tectonophysics* **255**, 203-209 (1996).
- 313 20. Kawabata, K., Tanaka, H. & Kimura, G. Mass transfer and pressure solution in  
314 deformed shale of accretionary complex: examples from the Shimanto Belt, southwest  
315 Japan. *J. Struct. Geol.* **29**, 697-711 (2007).

- 316 21. Fagereng, Å. in *Geology of the Earthquake Source: A Volume in Honour of Rick*  
317 *Sibson* (eds. Fagereng, Å., Toy, V.G. & Rowland, J.V.), 55-76 (Geol. Soc. London,  
318 2011).
- 319 22. Fagereng, Å. & Cooper, A.F. The metamorphic history of rocks buried, accreted and  
320 exhumed in an accretionary prism: an example from the Otago Schist, New Zealand. *J.*  
321 *Metamorph. Geol.* **28**, 935-954 (2010).
- 322 23. Bos, B. & Spiers, C. J. Frictional-viscous flow of phyllosilicate-bearing fault-rock:  
323 microphysical model and implications for crustal strength profiles. *J. Geophys. Res.*  
324 **107**, B2, 2028 (2002).
- 325 24. Niemeijer, A. & Spiers, C.J. in *High-Strain Zones: Structure and Physical*  
326 *Properties* (eds. Bruhn, D. & Burlini, L.), 303-327 (Geol. Soc. London, 2005).
- 327 25. Den Hartog, S.A.M. & Spiers, C.J. A microphysical model for fault gouge friction  
328 applied to subduction megathrusts. *J. Geophys. Res.* **119**, 1510-1529 (2014).
- 329 26. Molnar, P. & England, P. Temperatures, heat flux and frictional stress near major  
330 thrust faults. *J. Geophys. Res.* **95**, 4833-4856 (1990).
- 331 27. Den Hartog, S.A.M., Saffer, D.M. & Spiers, C.J. The roles of quartz and water in  
332 controlling unstable slip in phyllosilicate-rich megathrust fault gouges. *Earth Planets*  
333 *Space* **66**, doi:1186/1880-5981-66-78 (2014).
- 334 28. Den Hartog, S.A.M., Niemeijer, A.R. & Spiers, C.J. Friction on subduction  
335 megathrust faults: Beyond the illite-muscovite transition. *Earth Planet. Sci. Lett.* **373**, 8-  
336 19 (2013).

- 337 29. Van Diggelen, E.W.E., De Bresser, J.H.P., Peach, C.J. & Spiers, C.J. High shear  
338 strain behaviour of synthetic muscovite fault gouges under hydrothermal conditions. *J.*  
339 *Struct. Geol.* **32**, 1685-1700 (2010).
- 340 30. Den Hartog, S.A.M. & Spiers, C.J. Influence of subduction zone conditions and  
341 gouge composition on frictional slip stability of megathrust faults. *Tectonophysics* **600**,  
342 75-90 (2013).
- 343 31. Niemeijer, A.R., Spiers, C.J. & Peach, C.J. Frictional behaviour of simulated quartz  
344 fault gouges under hydrothermal conditions: Results from ultra-high strain rotary shear  
345 experiments. *Tectonophysics* **460**, 288-303 (2008).
- 346 32. Dieterich, J. H. Modeling of rock friction: 1. Experimental results and constitutive  
347 equations. *J. Geophys. Res.* **84**, 2161-2168 (1979).
- 348 33. Marone, C. Laboratory-derived friction laws and their application to seismic  
349 faulting. *Annu. Rev. Earth Planet. Sci.* **26**, 643-696 (1998).
- 350 34. Scholz, C. H. Earthquakes and friction laws. *Nature* **391**, 37-42 (1998).
- 351 35. Syracuse, E.M., van Keken, P.E. & Abers, G.A. The global range of subduction  
352 zone thermal models. *Phys. Earth. Planet. Inter.* **183**, 73-90 (2010).
- 353 36. Gao, X. & Wang, K. Strength of stick-slip and creeping subduction megathrusts  
354 from heat flow observations. *Science* **345**, 1038-1041 (2014).
- 355 37. Tester, J.W., Worley, W.G., Robinson, B.A., Grigsby, C. & Feerer, J.L. Correlating  
356 quartz dissolution kinetics in pure water from 25 to 625 °C. *Geochim. Cosmochim. Acta*  
357 **58**, 2407-2420 (1994).

- 358 38 Hashimoto, Y., Nakaya, T., Ito, M. & Kimura, G. Tectonolithification of sandstone  
359 prior to the onset of seismogenic subduction zone: Evidence from tectonic mélange of  
360 the Shimanto Belt, Japan. *Geochem. Geophys. Geosyst.* **7**, Q06013 (2006).
- 361 39. Moore, J. C., Rowe, C. D. & Meneghini, F. in *The Seismogenic Zone of Subduction*  
362 *Thrust Faults* (eds. Dixon, T. H. & Moore, J. C.), 288-315 (Colombia University Press,  
363 2007).
- 364 40. Wallace, L. M. *et al.* Slow slip near the trench at the Hikurangi subduction zone,  
365 New Zealand. *Science* **353**, 701-704 (2016).
- 366 41. Dragert, H., Wang, K. & James, T. A silent slip event on the deeper Cascadia  
367 subduction interface. *Science* **292**, 1525-1528.
- 368 42. Obara, K., Hirose, H., Yamamizu, F. & Kasahara, K. Episodic slow slip events  
369 accompanied by non-volcanic tremors in southwest Japan subduction zone. *Geophys.*  
370 *Res. Lett.* **31**, L23602 (2004).
- 371 43. Liu, Y. & Rice, J. R. Aseismic slip transients emerge spontaneously in three-  
372 dimensional rate and state modelling of subduction earthquake sequences. *J. Geophys.*  
373 *Res.* **110**, B08307 (2005).
- 374 44. McCrory, P. A., Hyndman, R. D. & Blair, J. L. Relationship between the Cascadia  
375 fore-arc mantle wedge, nonvolcanic tremor, and the downdip limit of seismogenic  
376 rupture. *Geochem. Geophys. Geosyst.* **15**, 1071-1095 (2014).
- 377 45. Saffer, D. M. & Wallace, L. M. The frictional, hydrologic, metamorphic and thermal  
378 habitat of shallow slow earthquakes. *Nat. Geosci.* **8**, 594-600 (2015).
- 379 46. Ruff, L. Do trench sediments affect great earthquake occurrence in subduction  
380 zones? *Pure Appl. Geophys.* **129**, 263-282 (1989).

381 47. Wesnousky, S.G. Predicting the endpoints of earthquake ruptures. *Nature* **444**, 358-  
382 360 (2006).

383 48. Fagereng, Å. Wedge geometry, mechanical strength, and interseismic coupling of  
384 the Hikurangi subduction thrust, New Zealand. *Tectonophysics* **507**, 26-30 (2011).

385 49. Knipe, R. J. Deformation mechanisms – Recognition from natural tectonites. *J.  
386 Struct. Geol.* **11**, 127-146 (1989).

387 50. Hicks, S. P. *et al.* The 2010  $M_w$  8.8 Maule, Chile earthquake: Nucleation and  
388 rupture propagation controlled by a subducted topographic high. *Geophys. Res. Lett.* **39**,  
389 L19308 (2012).

390

391 ACKNOWLEDGEMENTS: Initial work on this project was funded through NRF  
392 Incentive Funding for Rated Researchers to Å.F. while at the University of Cape Town.  
393 We thank Christel Tinguely (Cape Town) and Duncan Muir (Cardiff) for  
394 microprobe/SEM assistance, and Andrew Cross and three anonymous reviewers for  
395 constructive reviews that significantly improved the manuscript.

396 AUTHOR CONTRIBUTIONS: Both authors contributed to designing the study,  
397 making the calculations, and writing the paper. Å.F. provided the microstructural  
398 observations.

399 COMPETING INTERESTS: The authors declare that they have no competing financial  
400 interests.

401 AUTHOR INFORMATION: Correspondence and requests for materials should be  
402 addressed to Å. Fagereng (email: FagerengA@cardiff.ac.uk).

403 **Figure captions**

404 Figure 1: Example of pressure solution microstructures in a sample from the Chrystalls  
405 Beach Complex, New Zealand.

406 **a**, Photograph of outcrop-scale mélange shear zone with sandstone lenses in cleaved  
407 mudstone matrix. **b**, Photomicrograph (plane-polarised light) of sample from mélange  
408 matrix, cleavage wraps around quartz clasts. **c**, Close-up of cleavage seams, rectangle  
409 shows location of element maps of Si and Al; warm and cold colours show high and  
410 low relative abundance, respectively. **d** Backscatter electron image of quartz clasts in  
411 phyllosilicate matrix, accompanied by composite element map in **e**. **f**, Model  
412 microstructure where matrix (grey) deforms by frictional sliding along foliations  
413 (dashed lines), and clasts (black) deform by pressure solution<sup>25</sup>. All panels show dextral  
414 sense of shear.

415 Figure 2: Strength curves calculated along a subduction thrust interface with properties  
416 representative of the northern Hikurangi margin.

417 The pore fluid factor  $\lambda = P_f/\sigma_v$ , where  $P_f$  is pore fluid pressure and  $\sigma_v$  is vertical stress, is  
418 moderate (0.8) in **a** and high (0.95) in **b**. The curves labelled 'microphysical model'  
419 represent the strength of a fault where deformation occurs by slip on phyllosilicate  
420 surfaces and pressure solution of intervening quartz. Microphysical model predictions  
421 depend on grain size,  $D$ , and shear zone thickness,  $w$ , as shown in the legend, and  
422 thermal profiles as shown in **c**, including initial thermal structure where the frictional  
423 coefficient,  $\mu$ , is 0.6. Supplementary Table S1 reports the full list of parameters.

424

425 Figure 3: Relations between slip velocity and frictional behaviour

426 **a**, Schematic relationship between friction coefficient and strain rate in the  
427 microphysical model used here, indicating a change from velocity-strengthening to  
428 velocity-weakening at high strain rate<sup>25</sup>. **b**, quantifies friction coefficient at a fixed  
429 depth, as a function of strain rate or shear zone width at a fixed slip velocity, whereas **c**  
430 combines calculations of friction coefficient vs. strain rate at all considered depths, to  
431 depict the depth-dependent strain rates where a change from velocity-strengthening to  
432 velocity-weakening is predicted (parameters as in Fig. 2).

433 Figure 4: Representations of the effect of frictional-viscous flow on megathrust seismic  
434 style.

435 Subduction interfaces related to smooth (**a**) and rugged (**b**) topography on subducting  
436 oceanic crust. Inferred transient and steady-state strain rate variations along these  
437 interfaces are shown below, as is the inferred depth vs. creep strength profile as based  
438 on Fig. 2 and down-dip variation in shear zone width.

439

440    **Method**

441    **Element Maps**

442       Element maps (Fig. 1c,d,e; Supplementary Figure 2) were plotted from energy  
443       dispersive spectroscopy (EDS) data, which give relative abundance of elements,  
444       measured on a carbon-coated, 30  $\mu\text{m}$  thick sample. Maps in Fig. 1c were collected using  
445       an electronprobe microanalyser at the University of Cape Town, with beam conditions  
446       of 15 kV, 18.5 nA, 12 ms dwell time, and spot size of 1  $\mu\text{m}$ . Electron backscatter  
447       images in Fig. 1d, and map in Fig. 1e were acquired using a Zeiss Sigma HD scanning  
448       electron microscope in the School of Earth & Ocean Sciences at Cardiff University. The  
449       EDS data for these element maps were acquired with an beam accelerating voltage of 20  
450       kV, nominal beam current of 4.7 nA, and a 20 ms dwell time. Resulting pixels are  
451       approximately 1  $\mu\text{m}$ .

452    **Pressure-temperature estimates**

453       To calculate the shear stress predicted by the microphysical model as a function of  
454       depth, approximations of temperature,  $T$ , and effective normal stress,  $\sigma_n'$ , as functions  
455       of depth are required. Because the subduction thrust interface is gently dipping,  $\sigma_n'$  is  
456       approximated as the effective vertical stress<sup>51,52</sup> so that

$$457 \quad \sigma_n' = \rho g z (1 - \lambda) \quad (1)$$

458 where  $\rho$  is the average density of overlying rock, taken as 2650 kg/m typical of  
 459 quartzofeldspathic rocks,  $g$  is gravitational acceleration,  $\lambda$  is pore fluid factor as defined  
 460 in the main text, and  $z$  is depth.

461 Temperature (in °C) is calculated according to the analytical derivation of Molnar  
 462 and England<sup>26</sup>, as also applied to the Hikurangi margin by McCaffrey et al.<sup>53</sup>, that sums  
 463 advective, radiogenic, and shear heating terms where

$$464 \quad T = \frac{K_m}{SK_s} \frac{T_0 z}{\sqrt{\pi \kappa (t_0 + t_s)}} + \frac{A_r z^2}{2SK_s} + \frac{\tau V z}{SK_s} \quad (2)$$

465 in which the dimensionless parameter  $S$  is defined as

$$466 \quad S = 1 + b \frac{K_m}{K_s} \sqrt{\frac{V z \sin \delta}{\kappa}} \quad (3)$$

467 In these formulations,  $K_m$  and  $K_s$  are mantle and accretionary prism conductivities,  
 468 respectively,  $T_0$  is temperature at the base of the lithosphere,  $\kappa$  is thermal diffusivity,  $t_0$   
 469 is the age of the subducting oceanic crust at the trench,  $A_r$  is average radioactive heat  
 470 production rate in the forearc materials,  $\tau$  is shear stress, and  $b$  is a geometrical factor.  $t_s$   
 471 is the time to subduct the slab to depth  $z$ , approximated as  $t_s = z / (V \sin \delta)$  where  $V$  is  
 472 slip velocity, assuming the megathrust accommodates the trench-normal component of  
 473 the plate convergence vector, and  $\delta$  is the average dip angle of the subduction thrust  
 474 interface. Values for all the above parameters are listed in Supplementary Table 1. To  
 475 obtain the shear heating term in the initial thermal structure,  $\tau$  is estimated as  $\sigma_n'$   
 476 multiplied by a frictional coefficient of  $\mu = 0.6$ , estimating the lower end of the Byerlee

477 range<sup>54</sup>. After calculating shear stress according to the microphysical model, the  
478 calculated shear stress as a function of depth is used to re-calculate the thermal  
479 structure, which is then used to re-calculate shear stress. The change in thermal structure  
480 from the first calculation to calculations involving shear stresses from the microphysical  
481 model can be seen in Fig. 2c.

482 **Temperature-dependent mono-mineralic friction**

483 Values for the friction coefficient for phyllosilicates were determined assuming  
484 the dominant phyllosilicate mineral to be illite and muscovite at temperatures below and  
485 above 300 °C, respectively, and by assuming that temperature rather than effective  
486 normal stress dominantly affects the friction coefficient. The friction coefficient of illite  
487 as a function of temperature was determined by fitting a linear trend line to a  
488 combination of the data by Tembe et al.<sup>55</sup> at 20°C and the data of Den Hartog et al.<sup>27</sup> at  
489 200, 350 and 500°C, all representing final friction values (at 9.21 and ~40 mm shear  
490 displacement, respectively) at a sliding velocity of 1 µm/s. Note that the sliding velocity  
491 at ~40 mm shear displacement in the experiments of Den Hartog et al.<sup>27</sup> was 10 µm/s,  
492 and we thus recalculated it to 1 µm/s using the value for  $\Delta\mu/\Delta\ln V$ , or  $(a-b)$ , for a  
493 velocity step from 10 to 1 µm/s obtained in the same experiment. Similarly, the friction  
494 coefficient of muscovite as a function of temperature was determined by fitting two  
495 linear trendlines (joining at 600°C) to the data by Den Hartog et al.<sup>28</sup> at 200, 400 and  
496 600°C and the data by Van Diggelen et al.<sup>29</sup> at 400, 500 and 700°C. These data  
497 represent close to final friction coefficients, those by Den Hartog et al.<sup>28</sup> taken at a shear  
498 strain of 50 and recalculated for 1 µm/s by the method described for illite and those by  
499 Van Diggelen et al.<sup>29</sup> reported for the 0.5 µm/s step, which occurred at near steady state

500 friction. The resultant empirical function for phyllosilicate friction coefficient,  $\mu_{ph}$ ,  
 501 becomes

$$502 \quad \mu_{ph} = \begin{cases} 0.320 + 9.10 \times 10^{-4}T, & T < 300^\circ\text{C} \\ 0.300 + 6.18 \times 10^{-4}T, & 300^\circ\text{C} \leq T < 600^\circ\text{C} \\ 1.997 - 2.24 \times 10^{-3}T, & T \geq 600^\circ\text{C} \end{cases} \quad (4)$$

503 This definition for the phyllosilicate friction coefficient was used to construct the  
 504 strength profiles for pure phyllosilicates and as input to the microphysical model.

505 The friction coefficient of quartz, for plotting the frictional strength of mono-  
 506 mineralic quartz aggregates in Fig. 2a,b, is estimated based on the room temperature  
 507 data of Tembe et al.<sup>55</sup>, data at 140 °C of Den Hartog and Spiers<sup>30</sup> and the data at 400-  
 508 600 °C of Niemeijer et al.<sup>31</sup>. Based on similar arguments as for creating an empirical  
 509 function of phyllosilicate friction as a function of temperature, we obtain a function for  
 510 quartz friction,  $\mu_{qtz}$ :

$$511 \quad \mu_{qtz} = \begin{cases} 0.750 - 1.04 \times 10^{-4}T, & T < 500^\circ\text{C} \\ 1.41 - 1.43 \times 10^{-3}T, & T \geq 500^\circ\text{C} \end{cases} \quad (5)$$

## 512 **Microphysical model by Den Hartog and Spiers<sup>25</sup>**

513 The microphysical model used to calculate the strength profiles (Fig. 2) was  
 514 derived by Den Hartog and Spiers<sup>25</sup>. The model describes the steady state frictional  
 515 behaviour of sheared illite-quartz mixtures, and assumes a matrix-supported shear zone  
 516 consisting of phyllosilicates and quartz clasts (Supplementary Figure 3). The quartz

517 clasts are uniformly distributed, arranged such that horizontal rows of clasts overlap. On  
518 average, the phyllosilicates are aligned parallel to Y-shear bands, but locally  
519 anastomose around the rigid clasts. Note that the Y-shear bands considered in the model  
520 by Den Hartog and Spiers<sup>25</sup> will on average be parallel to the megathrust interface,  
521 which implies that foliation that is parallel to these shear bands, described as  
522 “horizontal” in the model, will be gently dipping in the megathrust setting.

523 Within the model microstructure, shear deformation occurs either within the “clast  
524 body” zones containing a horizontal phyllosilicate foliation and quartz clasts (Type B  
525 zones, Supplementary Figure 3) or in the “clast overlap” regions containing  
526 anastomosing phyllosilicates and overlapping quartz clast edges (Type O zones,  
527 Supplementary Figure 3). The horizontal foliation in the Type B zones abuts against the  
528 quartz clasts, so that sliding on this foliation requires serial simple shear of the clast  
529 “bodies”. Shear of the clasts is assumed to occur by thermally activated deformation. By  
530 contrast, in the Type O zones, the foliation anastomoses around the clast “overlaps”. In  
531 these zones, deformation can occur either by slip on the phyllosilicates at the zone  
532 margins accommodated by shearing of the clast overlaps, or by slip on the curved  
533 foliation accompanied by dilatation at extensional clast-matrix interface sites. Sliding on  
534 the foliation is assumed to be a purely frictional process, which implies that slip on the  
535 curved foliation will not occur unless a critical value of the macroscopic shear stress,  
536  $\tau_{dil}$ , is attained. When slip is activated, it will cause dilatation and porosity development.  
537 Den Hartog and Spiers<sup>25</sup> assumed that developing porosity concentrates at the  
538 extensional quartz-illite interfaces (Supplementary Figure 3), resulting in a decrease in  
539 the clast overlap distance, and hence in the mean inclination of the curved foliation.  
540 This in turn causes a decrease in the rate of dilation per unit horizontal displacement on

541 the inclined foliation, i.e. a decrease in the dilatation angle  $\psi_{dil}$ , with increasing porosity.  
542 Den Hartog and Spiers<sup>25</sup> assumed that the appearance of porosity, via clast/matrix  
543 debonding, initiates compaction by thermally activated deformation of the clasts, which  
544 accelerates as porosity increases. At steady state, dilation due to slip on the curved  
545 foliation and compaction by the thermally activated mechanism must balance. This  
546 competition between dilatation and compaction is of key importance since it will lead to  
547 higher steady state porosities, a flatter foliation and lower frictional strength as sliding  
548 velocity increases, and hence to velocity-weakening slip. This as opposed to non-  
549 dilatant deformation, where the serial nature of deformation implies that the velocity-  
550 dependence of friction is governed by thermally activated deformation of the quartz  
551 clasts which is by definition velocity-strengthening. Dilatation, when active, is assumed  
552 to continue until a limiting or critical state porosity is reached.

553 The model by Den Hartog and Spiers<sup>25</sup> does not strictly apply to muscovite.  
554 However, in the absence of a microphysical model for the steady state frictional  
555 behaviour of muscovite-quartz fault gouge, and since muscovite-quartz gouge shows  
556 broadly similar behaviour to illite-quartz gouge<sup>28</sup>, we have applied this model also at  
557 temperatures >300°C where muscovite is expected to be the dominant phyllosilicate.

## 558 Model calculations

559 The reader is referred to Den Hartog and Spiers<sup>25</sup> for the derivation of the  
560 equations governing the steady state frictional behaviour of the model microstructure  
561 shown in Supplementary Figure 3 and described below.

562 Den Hartog and Spiers<sup>25</sup> derive their equations for the unit cell shown in  
563 Supplementary Figure 3b, which has a horizontal dimension equal to horizontal clast  
564 spacing:

565 
$$L = \frac{k_f \pi D^2}{(D - x_0) f_{qtz}} \quad (6)$$

566 where  $k_f$  is a factor accounting for clast shape,  $D$  is grain size (clast diameter),  $f_{qtz}$   
567 is the volume fraction of quartz clasts, and  $x_0$  is the vertical overlap of the clasts at zero  
568 porosity defined by Den Hartog and Spiers<sup>25</sup> as

569 
$$x_0 = D \left( 1 - \sqrt{\frac{k_f \pi}{2 f_{qtz}}} \right) \quad (7)$$

570 As porosity,  $\phi$ , increases due to dilatational slip on the curved foliation, this  
571 overlap decreases from  $x_0$  to an instantaneous value  $x$  according to the relation  $x = (x_0 -$   
572  $\phi D]/(1-\phi)$ . The decrease in overlap in turn leads to a decrease in the width,  $d$ , of  
573 overlapping clast segments (Supplementary Figure 3b), given  $d = 2\sqrt{(Dx-x^2)}$ .

574 During non-dilatant deformation at low slip velocities and/or high temperatures,  
575 thermally activated shear deformation of the quartz clasts will be easy. The total  
576 resistance to slip on the horizontal foliation will then be lower than the shear stress to  
577 activate slip and dilatation on the anastomosing foliation. Under these conditions, Den  
578 Hartog and Spiers<sup>25</sup> assumed that non-dilatant deformation takes place by the parallel  
579 processes of (i) slip on the horizontal foliation with serial shear of the clast bodies in the  
580 B zones of the microstructure plus (ii) slip on the horizontal phyllosilicates with serial

581 shear of clast overlaps at the margin of the O zones. Equilibrium between the shear  
 582 stresses supported by the B and O zones ( $\tau_B$  and  $\tau_O$ , respectively) requires  $\tau_m = \tau_B = \tau_O$   
 583 where  $\tau_m$  is the macroscopic shear stress. The shear stresses in the B and O zones were  
 584 derived by Den Hartog and Spiers<sup>25</sup>:

$$585 \quad \tau_B = \tau_{ph} \left( 1 - \frac{A_{qtz-b}}{LD} \right) + \tau_{qtz-b} \frac{A_{qtz-b}}{LD} \quad (8)$$

$$586 \quad \tau_O = \tau_{ph} \left( 1 - \frac{A_{qtz-o}}{LD} \right) + \tau_{qtz-o} \frac{A_{qtz-o}}{LD} \quad (9)$$

587 where  $\tau_{ph}$  is the shear stress needed to drive frictional slip on the horizontal  
 588 phyllosilicate foliation and  $\tau_{qtz-b}$  and  $\tau_{qtz-o}$  are those needed to drive thermally activated  
 589 clast body and overlap deformation, respectively.  $A_{qtz-b}$  represents the average horizontal  
 590 area occupied by a single clast body within zone B of the unit cell, and is given  $A_{qtz-b} =$   
 591  $[(\frac{1}{4}\pi D^2 - 2A'_{seg})D]/(D - 2x)$ , where  $A'_{seg} = [16x^2(D - x) + 3x^3]/[12\sqrt{(Dx - x^2)}]$  (Ref. 56)  
 592 is the area of an individual clast segment located in the overlap zone of the cell in the  
 593 plane of Supplementary Fig. 3 and  $A_{qtz-o} = dD = 2D\sqrt{(Dx - x^2)}$  is the area over which the  
 594 overlap is displaced by slip at its base. Note that  $\tau_{ph} = \mu_{ph}\sigma_n'$  where  $\mu_{ph}$  is defined by  
 595 equation (4).

596 The parallel shear processes (i, ii) operating in the O and B zones mean that the  
 597 total, measured shear strain rate during non-dilatant deformation is  $\dot{\gamma}_m = \dot{\gamma}_B + \dot{\gamma}_O$ , where  
 598  $\dot{\gamma}_B$  and  $\dot{\gamma}_O$  denote the shear strain rate contributed to the unit cell by each zone  
 599 respectively (i.e.  $\dot{\gamma}_B$  and  $\dot{\gamma}_O$  are determined by taking into account the thickness of the  
 600 B or O zone relative to the unit cell thickness). Note that the serial coupling of rate-

601 independent slip on the phyllosilicates with thermally activated deformation of clasts  
 602 implies that  $\dot{\gamma}_B = \dot{\gamma}_{qtz-b}$  and  $\dot{\gamma}_O = \dot{\gamma}_{qtz-o}$ , where,  $\dot{\gamma}_{qtz-b}$  and  $\dot{\gamma}_{qtz-o}$  are the shear strain  
 603 rate contributions to the unit cell due to thermally activated deformation of the clast  
 604 bodies and clast overlaps, respectively. Thermally activated deformation was assumed  
 605 to occur via pressure solution by Den Hartog and Spiers<sup>25</sup>, yielding:

$$606 \quad \dot{\gamma}_{qtz-b} = \frac{AI\tau_{qtz-b}\Omega}{RT} \frac{D-2x}{D(D-x)} \quad (10)$$

$$607 \quad \dot{\gamma}_{qtz-o} = \frac{2I\tau_{qtz-o}\Omega}{RT} \frac{1}{\sqrt{Dx-x^2}} \quad (11)$$

608 Where  $A$  is a shape factor,  $I$  is the product of the dissolution rate coefficient  $k_+$   
 609 and molar volume  $\Omega$  of quartz, and  $R$  is the gas constant.

610 Following Den Hartog and Spiers<sup>25</sup>, we obtained  $\tau_m$  as a function of  $\dot{\gamma}_m$ , by first  
 611 imposing  $\dot{\gamma}_m$ , defined as  $\dot{\gamma}_m = V/w$  where  $w$  is the shear zone width. We next solved  
 612  $\dot{\gamma}_m = \dot{\gamma}_B + \dot{\gamma}_O$  together with  $\tau_m = \tau_B = \tau_O$  to obtain  $\dot{\gamma}_B$  or  $\dot{\gamma}_{qtz-b}$ . We subsequently used  
 613  $\dot{\gamma}_{qtz-b}$  to determine  $\tau_{qtz-b}$  via equation (10). The value of  $\tau_{qtz-b}$  obtained, then yielded  $\tau_B$   
 614 =  $\tau_m$  through equation (8). Note that in the current calculations we prevented  $\dot{\gamma}_o$  from  
 615 taking a negative value in the non-dilatant regime<sup>57</sup>.

616 At high slip rates or low temperatures, thermally activated shear deformation of  
 617 the quartz clasts is difficult, leading to an increase in the total resistance to shear on the  
 618 horizontal foliation. In the model microstructure of Den Hartog and Spiers<sup>25</sup> this would

619 ultimately activate slip on the curved phyllosilicates in the overlap (O) zones of the  
 620 microstructure. The measured shear strength in that case is equal to that required to  
 621 activate slip on the anastomosing foliation,  $\tau_{dil}$ , derived by Den Hartog and Spiers<sup>25</sup> to  
 622 be

$$623 \quad \tau_{dil} = \left\{ \frac{\mu_{ph} (1 + \tan^2 \Psi_{fr})}{1 - \mu_{ph}^2 \tan^2 \Psi_{fr}} \right\} \sigma'_n \quad (12)$$

624 where  $\tan \Psi_{fr}$  is a straight line approximation of the curved foliation, i.e.

$$625 \quad \tan \Psi_{fr} = \frac{2(D - x_0) f_{qtz}}{k_f \pi D^2} x \quad (13)$$

626 Stress equilibrium between B and O zones means that in the dilatant case  $\tau_m = \tau_{dil}$   
 627  $= \tau_B = \tau_O$ . The total shear strain rate  $\dot{\gamma}_m$ , in turn, is given  $\dot{\gamma}_m = \dot{\gamma}_B + \dot{\gamma}_O + \dot{\gamma}_{dil}$ , or  
 628 equivalently  $\dot{\gamma}_m = \dot{\gamma}_{qtz-b} + \dot{\gamma}_{qtz-o} + \dot{\gamma}_{dil}$ , where  $\dot{\gamma}_{dil}$  is the shear strain rate contribution to  
 629 the unit cell by dilatant slip on the curved phyllosilicates. This mechanism produces an  
 630 associated dilational strain rate,  $\dot{\varepsilon}_{dil}$ , which Den Hartog and Spiers<sup>25</sup> defined following  
 631 the classical soil mechanics approach to granular flow, i.e.

$$632 \quad \dot{\varepsilon}_{dil} = \left( \frac{d\varepsilon_{dil}}{d\gamma_{dil}} \right) \frac{d\gamma_{dil}}{dt} = (\tan \Psi_{dil}) \dot{\gamma}_{dil} \quad (14)$$

633 Den Hartog and Spiers<sup>25</sup> defined the dilatation angle  $\Psi_{dil}$  as the steepest portion of  
 634 the curved, i.e. sinusoidal, foliation:

635                   
$$\tan \Psi_{dil} = \sqrt{\frac{\pi f_{qtz}}{2k_f}} - \frac{\pi}{2(1-\phi)} \quad (15)$$

636                  This angle ( $\Psi_{dil}$ ) decreases with increasing porosity, reaching zero at a limiting or  
 637          “critical state” porosity, defined  $\phi_c = x_0/D$  when  $x = 0$ .

638                  The porosity generated by dilatant slip will induce compaction by thermally  
 639          activated deformation of the quartz clasts at a rate  $\dot{\varepsilon}_{comp}$ . Taking compaction as positive,  
 640          the total, measured compaction strain rate is therefore given  $\dot{\varepsilon}_m = \dot{\varepsilon}_{comp} - \dot{\varepsilon}_{dil}$ . At  
 641          steady state, dilatation and compaction must balance, resulting in a steady state porosity  
 642          corresponding to the condition that  $\dot{\varepsilon}_m = 0$  or  $\dot{\varepsilon}_{comp} = \dot{\varepsilon}_{dil}$ . Following Den Hartog and  
 643          Spiers<sup>25</sup>,  $\dot{\varepsilon}_{comp}$  is given by:

644                   
$$\dot{\varepsilon}_{comp} = \frac{2I\sigma' \Omega}{RT} \frac{A_{pore}}{(D-x)DL} \quad (16)$$

645                  Compaction occurs by pressure solution transfer from compressively stressed  
 646          illite-quartz interfaces to debonded (dilated) interfaces (pore walls) with surface area  
 647           $A_{pore}$ , written  $A_{pore} = (A_{pore-c}/2)(\phi/\phi_c)^n$  where  $\phi_c$  and  $A_{pore-c}$  are the porosity and pore area  
 648          per clast at the critical state. Den Hartog and Spiers<sup>25</sup> derived that  $A_{pore-c} = (\pi D^2)/2$ .

649                  To calculate  $\tau_m$  as a function of  $\dot{\gamma}_m$  in the dilatant regime, we followed the  
 650          procedure by Den Hartog and Spiers<sup>25</sup> and incremented the porosity from 0 to  $\phi_c$  and  
 651          calculated the corresponding values of  $\tan \Psi_{dil}$  and  $\tan \Psi_{fr}$  using equations (15) and (13).  
 652          Using  $\tan \Psi_{fr}$ , equation (12) gives  $\tau_{dil}$ . The corresponding shear strain rate  $\dot{\gamma}_m$  is

653 calculated via  $\dot{\gamma}_m = \dot{\gamma}_{qtz-b} + \dot{\gamma}_{qtz-o} + \dot{\gamma}_{dil}$  and using the flow laws in equations (10) and  
 654 (11). Here,  $\dot{\gamma}_{dil}$  is obtained via equation (14) and using the steady state condition  
 655  $\dot{\varepsilon}_{comp} = \dot{\varepsilon}_{dil}$ , where  $\dot{\varepsilon}_{comp}$  is calculated using equation (16).

656 In our calculations, we assumed cylindrical quartz clasts ( $k_f = 0.25$ ) of either 10 or  
 657 100  $\mu\text{m}$  in diameter, taking up a volume fraction of 0.45. Following Den Hartog and  
 658 Spiers<sup>25</sup>, we assume that pressure solution is controlled by the interfacial reactions of  
 659 dissolution and precipitation and can be described using the empirical equation for the  
 660 dissolution rate coefficient provided by Tester et al.<sup>37</sup>:

$$661 k_+ = 276 \exp\left(\frac{-90100}{RT}\right) \quad (17)$$

662 with  $T$  in Kelvin. We used a shape factor  $A$  of  $\pi$  in our calculation of the clast body  
 663 shear strain rate, while a factor of 2 was used in the original model. We also follow the  
 664 assumption that the porosity can be characterised by an exponent  $n$  of 0.3 (Ref. 25).

665 To determine our shear strength versus depth profiles predicted by the  
 666 microphysical model, we selected  $\sigma_n'$ ,  $T$  and the corresponding  $\mu_{ph}$  at each depth. Using  
 667 this input, we obtained  $\tau_m$  as a function of  $\dot{\gamma}_m$  (incorporating both non-dilatant and  
 668 dilatant deformation) following the above procedure. We next used the assumed  
 669 subduction velocity of 40 mm/yr and shear zone thickness (1 to 100 m in the current  
 670 calculations) to select relevant  $\dot{\gamma}_m$  and determined  $\tau_m$  at that shear strain rate.

671 The result of our calculations, shown in Fig. 2, yield dilatant deformation at  
 672 shallow depths and low temperatures for the shear strain rates explored in this study.

673 With increasing depth and temperature shear deformation of the quartz clasts by  
674 pressure solution becomes easier, resulting in a transition to non-dilatant deformation.  
675 To illustrate this effect, we show the calculated values of  $\tau_{ph}$ ,  $\tau_{qz-b}$  (for non-dilatant  
676 shear), and the inferred shear stress as a function of depth, for the scenario where  $D$  is  
677 100  $\mu\text{m}$ ,  $w$  is 100 m, and  $\lambda$  is 0.95, in Supplementary Figure 4. For any given set of  
678 conditions, the transition to non-dilatant deformation depends on strain rate, and we plot  
679 the strain rate at which the transition occurs, as a function of depth, in Fig. 3c.

680 **Code and data availability**

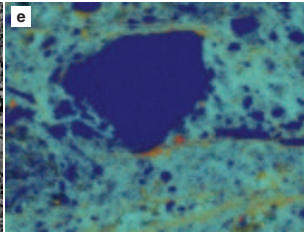
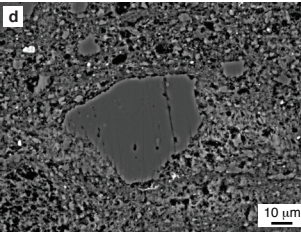
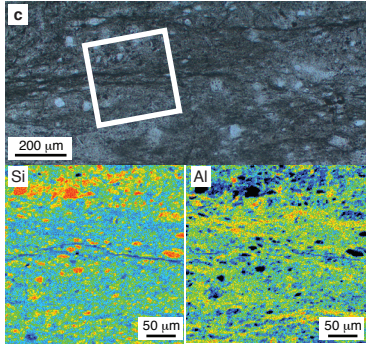
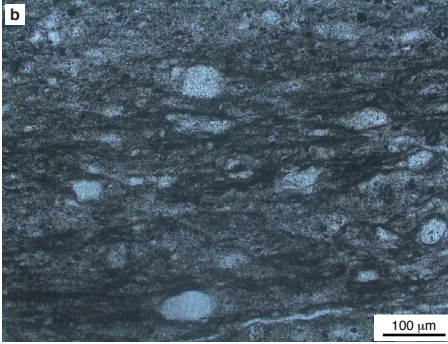
681 Code and additional data are available from the authors on request.

682 **Additional References**

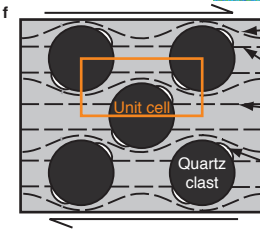
- 683 51. Lamb, S. Shear stresses on megathrusts: Implications for mountain building behind  
684 subduction zones. *J. Geophys. Res.* **111**, B07401, doi:10.1029/2005JB003916 (2006).
- 685 52. Wada, I., Wang, K., He, J. & Hyndman, R.D. Weakening of the subduction interface  
686 and its effects on surface heat flow, slab dehydration, and mantle wedge  
687 serpentization. *J. Geophys. Res.* **113**, B04402, doi:10.1029/2007JB005190 (2008).
- 688 53. McCaffrey, R., Wallace, L.M. & Beavan, J. Slow slip and frictional transition at low  
689 temperature at the Hikurangi subduction zone. *Nat. Geosci.* **1**, 316-320 (2008).
- 690 54. Byerlee, J. D. Friction of rocks. *Pure Appl. Geophys.* **116**, 615-626 (1978).
- 691 55. Tembe, S., Lockner, D.A. & Wong, T.-F. Effect of clay content and mineralogy on  
692 frictional sliding behaviour of simulated gouges: Binary and ternary mixtures of quartz,

- 693 illite and montmorillonite. *J. Geophys. Res.* **115**, B03416, doi:10.1029/2009JB006383
- 694 (2010).
- 695 56. Harris, J.W. & Stocker, H. *Handbook of Mathematics and Computational Science*.
- 696 (Springer-Verlag, New York, 1998).
- 697 57. Noda, H. Implementation into earthquake sequence simulations of a rate- and state-
- 698 dependent friction law incorporating pressure solution creep. *Geophys. J. Int.* **205**,
- 699 1108-1125 (2016).

700



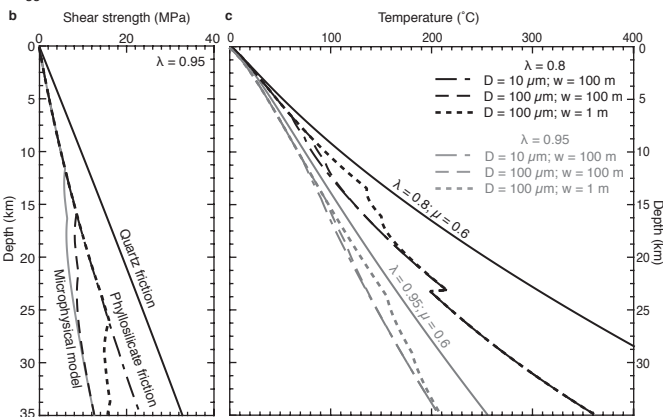
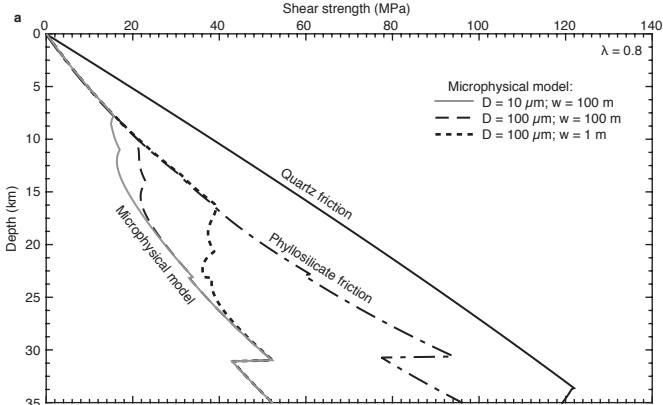
Si  
Al  
K  
Ti

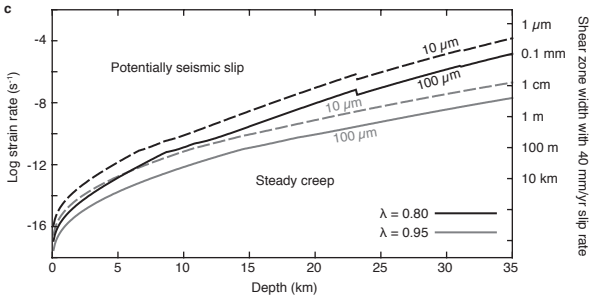
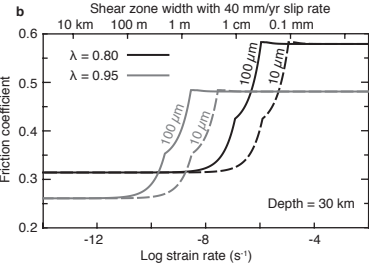
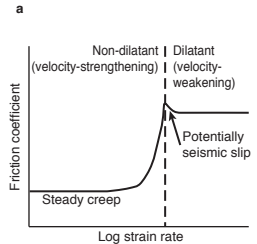


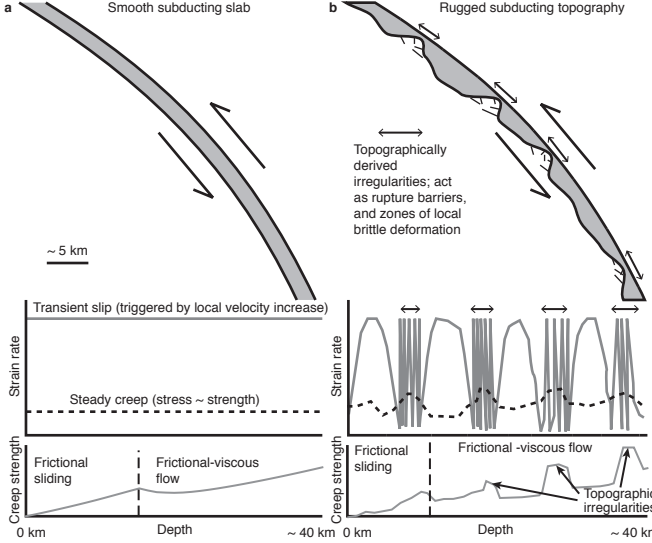
Curved phyllosilicate foliation:  
slip + dilatation or horizontal  
displacement of clast extremities

Horizontal phyllosilicate foliation:  
non-dilatant deformation + “flow”  
of quartz

Porosity at dilatant  
interfaces

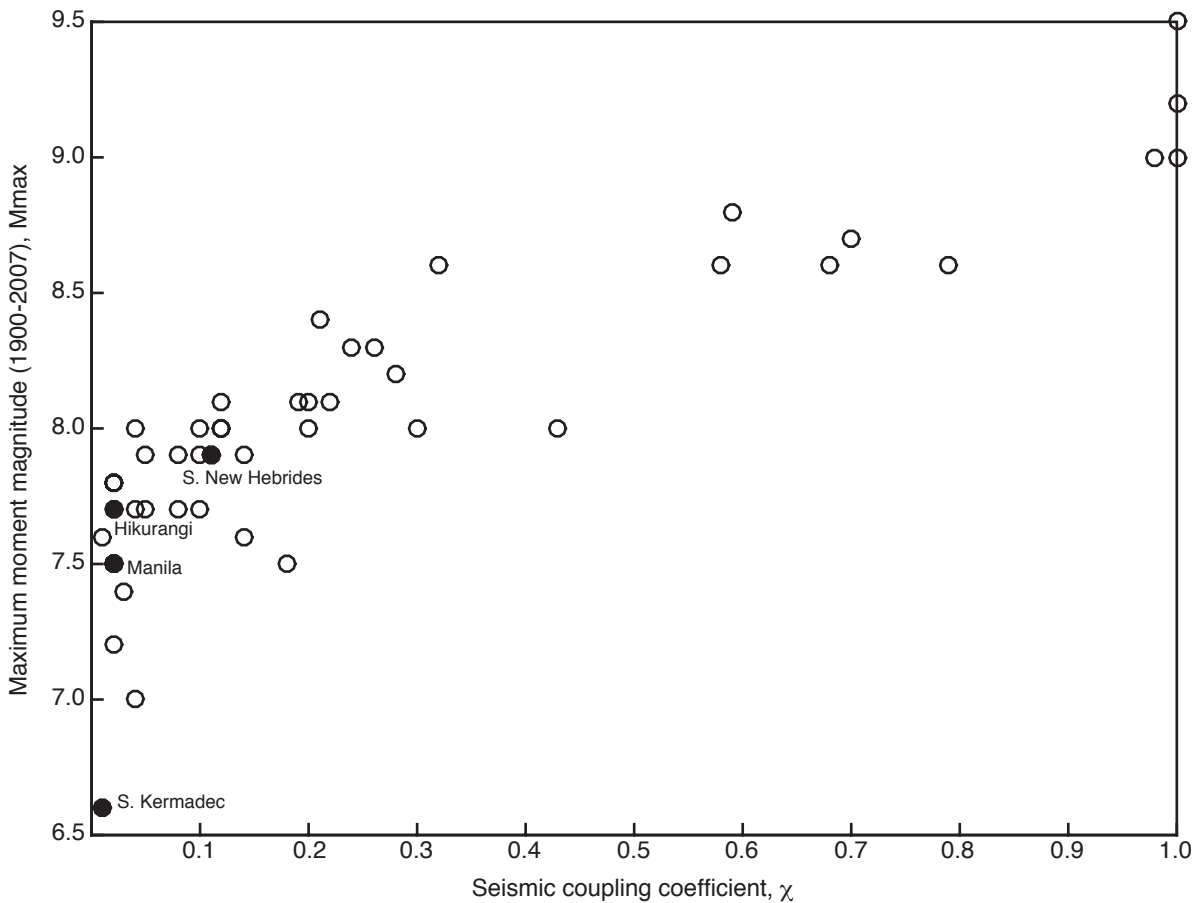






# Subduction megathrust creep governed by pressure solution and frictional-viscous flow

Åke Fagereng and Sabine A.M. den Hartog



**Supplementary Figure S1:** Plot of maximum moment magnitude,  $M_{max}$ , against seismic coupling coefficient,  $\chi$ . The data are from the compilation of Heuret et al. (2011), but limiting the maximum seismic coupling coefficient to 1.0. Examples in the main text are highlighted in solid circles. Note that Hikurangi in this plot includes both northern and southern Hikurangi, and that the  $M_w 7.7$  event in the Heuret et al. (2011) compilation may have included significant slip on a splay fault in the overlying accretionary prism (Wallace et al., 2009). Thus, both the coupling coefficient and the maximum magnitude may be overestimated. The southern Japan Trench is not highlighted despite being mentioned in the main text, as the area referred to is relatively small, but described in detail by Mochizuki et al. (2008); it is not added to retain consistency in the plotted data.

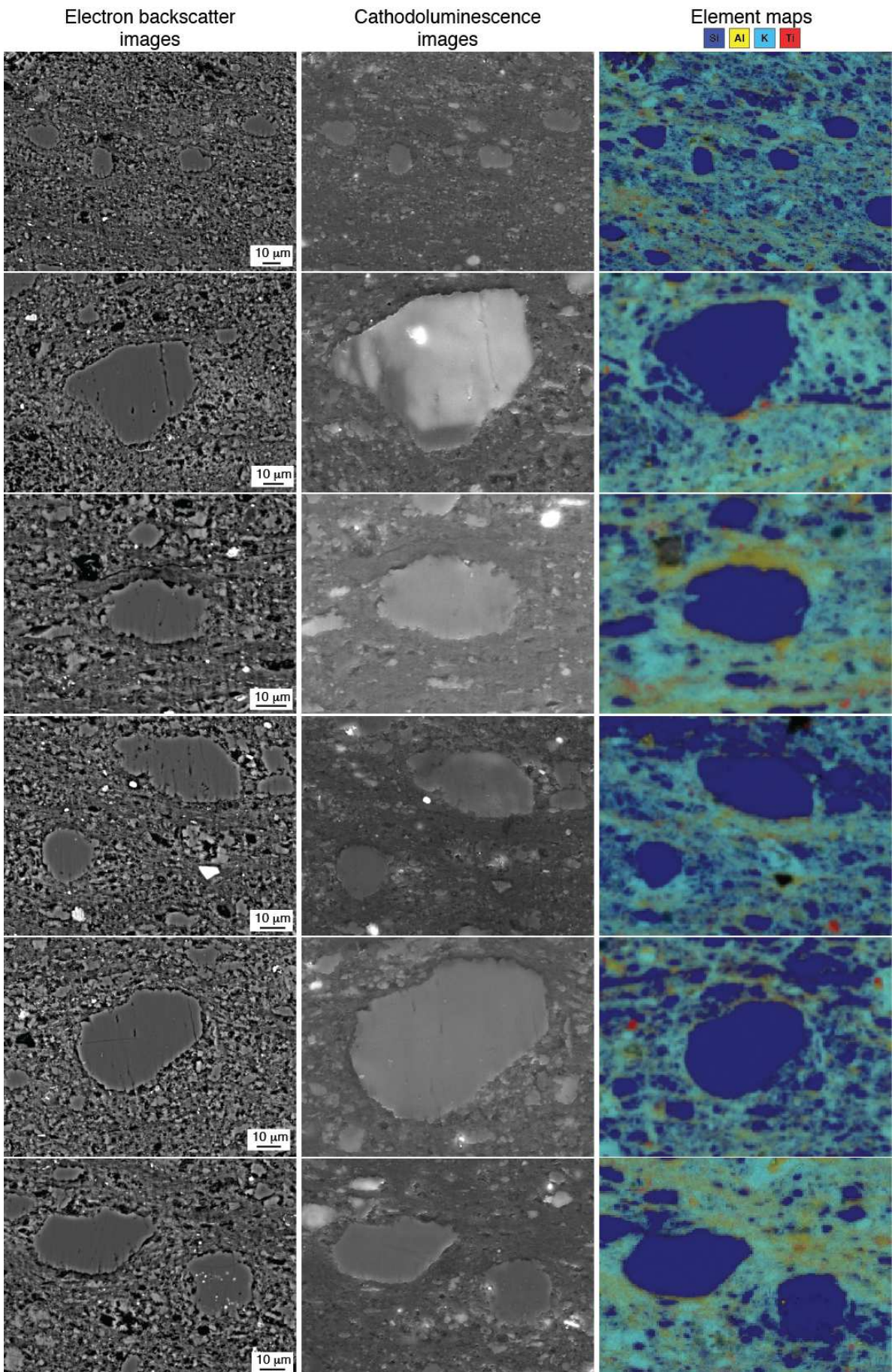
Data in Fig. S1 were compiled by Heuret et al. (2011) using data from the Harvard CMT catalogue for  $M_w \geq 5.5$  earthquakes from the 1976-2007 time period, including 1900-1975 for  $M_w \geq 7.0$  events in the Centennial catalogue of (Engdahl and Villaseñor, 2002). Earthquake locations were, if possible, relocated from the EHB catalogue of Engdahl et al. (1998). Thus, Heuret et al. (2011) extracted earthquakes with locations and, if available, nodal planes that align with the subduction thrust interface. From this data set, they defined the seismogenic zone of a number of megathrust interfaces, 49 for which they provide both  $M_{max}$  and  $\chi$ .

For the 49 subduction interfaces plotted in Fig. S1,  $M_{max}$  is the largest subduction thrust earthquake identified in the Heuret et al. (2011) compilation, i.e. that occurred between 1900 and 2007, and fell on the inferred megathrust interface. We note that overestimates may occur, through inclusion of poorly located events, that were not actually megathrust events, particularly events prior to 1964 that were not relocated in the EHB catalogue.

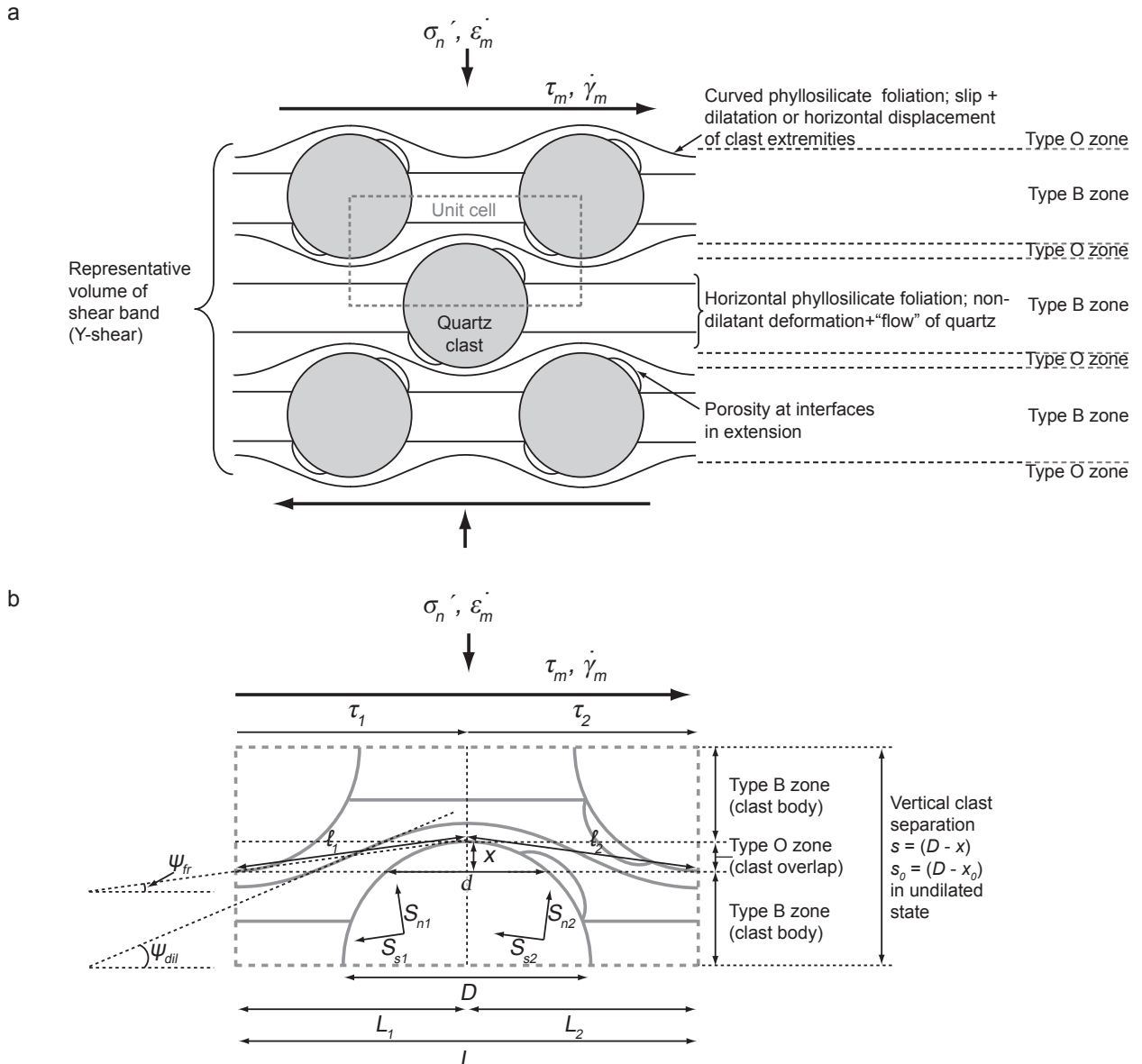
To calculate  $\chi$ , the amount of seismic slip and the rate of plate convergence must be estimated for each region. Defining seismic moment of a single earthquake as  $M_0 = GLWu$ , where  $G$  is shear modulus (50 GPa),  $L$  and  $W$  are the length and width of the rupture area, and  $u$  is average slip, the seismic slip rate for a time period  $T$  is  $v_s = Su/T = SM_0/(GLWT)$  (Brune, 1968). The seismic coupling coefficient,  $\chi$ , can be defined as the ratio of  $v_s$  to the subduction velocity as defined by global plate kinematic models, and was calculated accordingly by Heuret et al. (2011).

## References

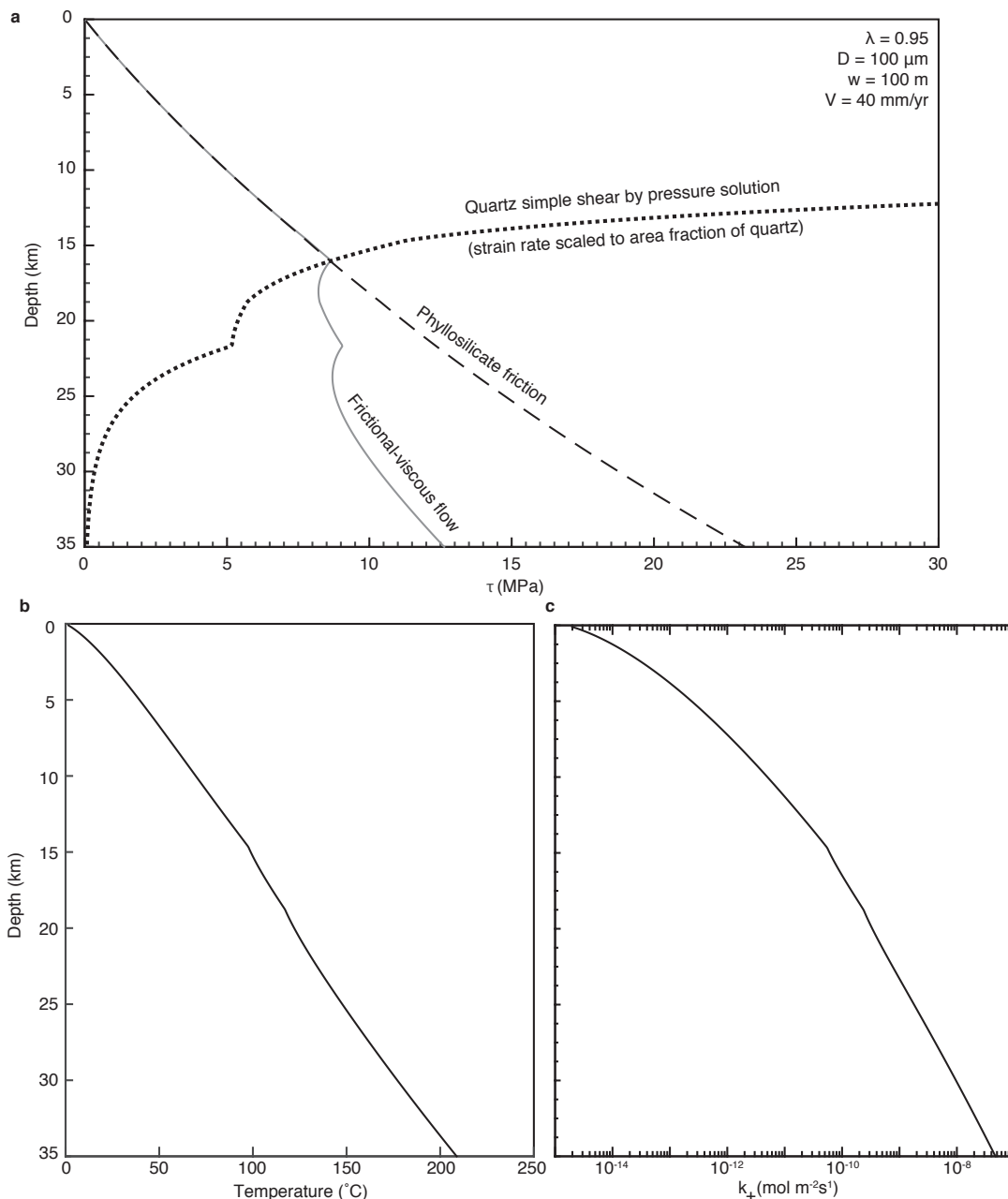
- Brune, J.N. Seismic moment, seismicity, and rate of slip along major fault zones. *J. Geophys. Res.* **73**, 777-784 (1968).
- Engdahl, R. & Villaseñor, A. Global seismicity: 1900-1999, in *International Handbook of Earthquake and Engineering Seismology, Part A* (eds Lee, W.H.K. et al.) 665-690 (Academic, Amsterdam, 2002).
- Engdahl, R., Van Der Hilst, R. & Buland, R. Global teleseismic earthquake relocation with improved travel times and procedures for depth determination. *Bull. Seismol. Soc. Am.* **88**, 722-743 (1998).
- Heuret, A., Lallemand, S., Funiciello, F., Pitomallo, C. & Faccenna, C. Physical characteristics of subduction interface type seismogenic zones revisited. *Geochem. Geophys. Geosyst.* **12**, Q01004, doi: 10.1029/2010GC003230 (2011).
- Mochizuki, K., Yamada, T., Shinohara, M., Yamanaka, Y. & Kanazawa, T. Weak interplate coupling by seamounts and repeating  $M \sim 7$  earthquakes. *Science* **321**, 1194-1197.
- Wallace, L.M. et al. Characterising the seismogenic zone of a major plate boundary subduction thrust: the Hikurangi Margin, New Zealand. *Geochem. Geophys. Geosyst.* **10**, Q10006, doi: 10.1029/2009GC002610 (2009).



**Supplementary Figure S2:** Scanning electron microscope images of Chrystalls Beach sample. Minor pore space development in pressure shadows can be seen in BSE images in the left column, and silica enrichment in pressure shadows can be discerned from EDS maps in the right column. The middle column shows little CL variation within most quartz clasts.



**Supplementary Figure S3:** Model microstructure assumed for phyllosilicate-quartz gouge undergoing shear deformation. **a.** Shows the representative microstructure, and the definition of clast body zones (B), clast overlap zones (O), and the unit cell as referred to in the method, and originally defined by Den Hartog and Spiers (2014, 25 in main text). In this figure,  $\sigma_n'$  is the effective normal stress,  $\tau_m$  is the macroscopic shear stress,  $\dot{\gamma}_m$  is the macroscopic or imposed shear strain rate and  $\varepsilon_m$  is the macroscopic rate of compaction. **b.** Shows the definition of the microstructural variables; the key variables are referred to and defined in the Methods. Note that the curved foliation is drawn with an exaggerated amplitude for clarity. Figure taken from Den Hartog and Spiers (2014, Ref 25 in the main text).



**Supplementary Figure S4:** Figure showing details of calculated parameters, for the scenario where quartz clast size,  $D$ , is  $100 \mu\text{m}$ , shear zone width,  $w$ , is  $100 \text{ m}$ , and the pore fluid factor,  $\lambda$ , is  $0.95$ . **a.** calculated values of phyllosilicate frictional resistance,  $\tau_{ph}$ , shear stress required for simple shear of quartz clast bodies,  $\tau_{qz-b}$  (for non-dilatant shear), and the inferred shear stress for frictional-viscous flow at the given strain rate of  $v/w = 1.3 \times 10^{-11} \text{ s}^{-1}$ , as a function of depth. **b.** Temperature as a function of depth. **c.** Dissolution rate constant for quartz in water,  $k_+$ , as a function of depth.

**Supplementary Table S1** List of parameter values used in the calculations performed in this paper.

Parameter	Meaning	Value
<i>Temperature and stress</i>		
$A_r$	Average radiogenic heat production in the forearc	$10^{-6} \text{ W m}^{-3}$
$b$	Geometric constant	1.0
$K_m$	Mantle conductivity	$3.3 \text{ W m}^{-1} \text{ K}^{-1}$
$K_s$	Accretionary prism conductivity	$2.55 \text{ W m}^{-1} \text{ K}^{-1}$
$t_0$	Age of subducting oceanic crust at the trench	80 Ma
$T_0$	Temperature at the base of the lithosphere	1300 °C
$V$	Average fault slip rate	$40 \text{ mm yr}^{-1}$
$\delta$	Average dip of subduction thrust interface	15°
$\lambda$	Pore fluid factor	0.8 or 0.95
$\kappa$	Thermal diffusivity	$10^{-6}$
$\rho$	Average density above the shear zone	$2650 \text{ kg m}^{-3}$
<i>Microphysical model</i>		
$A$	Shape factor in the clast body shear strain rate equation	$\pi$
$D$	Clast diameter (grain size)	10 or 100 μm
$f_{qtz}$	Volume fraction of quartz	0.45
$k_f$	Constant depending on the 3-D clast shape, $\frac{1}{4}$ for cylinder	0.25
$k_+$	Dissolution rate coefficient	$= 276 \times \exp(-90100/[R \times T (\text{K})]) \text{ mol m}^{-2} \text{ s}^{-1}$
$n$	Exponent in relation describing pore area, pore shape evolution parameter	0.3
$R$	Universal gas constant	$8.31462 \text{ J mol}^{-1} \text{ K}^{-1}$
$w$	Average shear zone thickness	1 - 100 m
$\mu_{ph}$	Friction coefficient within phyllosilicates	0-300°C: $= 0.3199 + 9.101 \times 10^{-4} T (\text{°C})$ 300-600°C: $= 0.2997 + 6.180 \times 10^{-4} T (\text{°C})$ 600-700°C: $= 1.9967 - 2.244 \times 10^{-3} T (\text{°C})$
$\Omega$	Molar volume of quartz	$2.27 \times 10^{-5} \text{ m}^3 \text{ mol}^{-1}$